Continental Shelf Research 61–62 (2013) 85–97

Contents lists available at SciVerse ScienceDirect

Continental Shelf Research

journal homepage: www.elsevier.com/locate/csr

Research papers

# Tidal variability of lateral advection in a coastal plain estuary

N.B. Basdurak [a,*], A. Valle-Levinson [b]

[a] Bodega Marine Laboratory, University of California Davis, 2099 Westside Road, P.O. Box 247, Bodega Bay, CA 94923, USA
[b] Department of Civil and Coastal Engineering, University of Florida, 365 Weil Hall, P.O. Box 116580, Gainesville, FL 32611, USA

ARTICLE INFO

*Article history:*
Received 19 July 2012
Received in revised form
8 April 2013
Accepted 16 April 2013
Available online 30 April 2013

*Keywords:*
Lateral advection
Tidal asymmetry
Curvature effect
Coastal plain estuary
Cheasapeake bay

ABSTRACT

Tidal variability of lateral advection of momentum ($vu_y$, where $u$ and $v$ are along-estuary and lateral flows, respectively, and the subindex indicates differentiation with respect to the cross-estuary direction) was investigated in a coastal plain estuary with observations at Hampton Roads, which is the transition between the James River and Chesapeake Bay. Towed current velocity profiles and hydrographic profiles were captured during 9 expeditions in 2004 and 2005, to determine the intratidal and spatial changes in lateral advection of momentum and its contribution to along-channel flow. Curvature effects and lateral density gradients were important in driving lateral circulation and in modifying intratidal lateral advection of momentum. Lateral advection had the same order of magnitude as the baroclinic pressure gradient. Its contribution to the along-channel momentum balance was greatest during or just after peak flood and weakest at the end of ebb. During peak flood and peak ebb, the spatial distribution of $vu_y$ was seaward at the southern (left) side near surface and at the northern side (right) near bed (looking up-estuary), and landward in the rest of the channel. During slack periods the $vu_y$ structures were mostly landward. Observations were in good agreement with analytical model results during peak ebb and flood, but inconsistent during slack periods. The discrepancies between model results and field measurements can be attributed to bathymetry–density gradient interactions, which enhanced ebb-to-flood asymmetries in the along-channel and lateral flow.

Published by Elsevier Ltd.

## 1. Introduction

The traditional basis of studies on along-estuary hydrodynamics has been the linear momentum balance between the pressure gradient and friction. This idealization yields a two-layer gravitational circulation with seaward near-surface flow and landward flow underneath (e.g., Pritchard, 1956; Hansen and Rattray, 1965; Chatwin, 1976; Officer, 1976). However, real flow structures often exhibit laterally sheared circulation and other complex structures not captured by the linear model. The importance of nonlinear lateral ($vu_y$) and vertical ($wu_z$) advective terms (where $u$, $v$, and $w$ denote along-channel, lateral, and vertical components of flow, respectively, and the subindices indicate differentiation with respect to that variable) to the momentum balance has been recently emphasized (e.g., Lerczak and Geyer, 2004; Huijts et al., 2009; Scully et al., 2009; Cheng and Valle-Levinson, 2009; Basdurak and Valle-Levinson, in press).

Lerczak and Geyer (2004) showed that the nonlinear advective term can actually be larger than the longitudinal pressure gradient in the along-channel momentum equation, and reinforce the two-layered circulation, particularly for weakly stratified estuaries. Scully et al. (2009) also showed that the nonlinear advective terms contribute to the subtidal along-channel momentum balance at leading order, driving a landward flow near bed. Furthermore, Lerczak and Geyer (2004) and Scully et al. (2009) found advective terms to be strongest near peak flood. Additionally, Huijts et al. (2009) separated subtidal along-channel flow into components induced by different mechanisms, and found that observed patterns were similar to those induced by nonlinear advective terms in the analytical model. Cheng and Valle-Levinson (2009) suggested that nonlinear advection drove vertically sheared net flow and could not be ignored in narrow and deep estuaries under weak vertical mixing. Zitman and Schuttelaars (2012) presented a condition which can be used beforehand as an indicative whether the magnitude of contribution of advective terms are in leading order, and showed that the theoretical approaches have to be made with great care.

The above studies are strictly theoretical and have yet to be verified by observations. Moreover, most of these studies have focused on the dynamics of subtidal flows but there is still a rudimentary understanding of the influence of lateral advective terms on intratidal dynamics. This study provides observational evidence that supports theoretical results. It documents intratidal variability in $vu_y$, and shows that the asymmetries in $vu_y$ play an important role in modifying the along-channel flow. The objectives

* Corresponding author. Tel.: +1 707 875 1925.
*E-mail addresses:* nuvitber@gmail.com, nbbasdurak@ucdavis.edu, nuvitber@ufl.edu (N.B. Basdurak).

0278-4343/$ - see front matter Published by Elsevier Ltd.
http://dx.doi.org/10.1016/j.csr.2013.04.026

of this study are to: (1) examine with field observations the contribution of $vu_y$ to the momentum balance over a tidal cycle in comparison to other terms (e.g., baroclinic and barotropic pressure gradient, vertical mixing, Coriolis and longitudinal accelerations) in the along-channel direction; and (2) analyze the structure of $vu_y$ across the channel during different stages of the tidal cycle and under distinct river discharge and tidal forcing conditions (i.e. neap and spring cycles). These objectives are addressed with data collected in Hampton Roads, at the James River entrance in Chesapeake Bay.

## 2. Study area

Hampton Roads is located at the entrance to the James River estuary, which is the southernmost tributary of the Chesapeake Bay (Virginia; Fig. 1). The transect studied has a main channel with maximum depth of 20 m, located between 1 and 1.8 km from the left (looking landward) end (Fig. 1b,c). Shoals with depth of $<$ ~6 m, located on each side of the transect were not sampled because of navigation restrictions.

The James River estuary is a micro-tidal, partially mixed estuary with well-developed gravitational circulation forced by freshwater discharge and tides (Shen and Lin, 2006). The annual mean freshwater discharge gauged at Richmond is ~200 $m^3/s$. The highest monthly discharge occurs between February and April (~335 $m^3/s$), and the lowest in July and September (~95 $m^3/s$; U.S. Geological Survey, Hydrologic Unit Code 02080205, http://waterdata.usgs.gov/va/nwis/monthly). Tides are predominantly semidiurnal with $M_2$, $N_2$, and $S_2$, in order of importance, being the most energetic constituents. The interaction between $M_2$ and $S_2$ causes fortnightly variability between neap and spring tides, generating differences in the baroclinic pressure gradients, advective accelerations and friction (Valle-Levinson et al., 2000b). The maximum tidal amplitudes are 0.45 m and 0.20 m during spring and neap cycles, respectively.

## 3. Data collection and processing

Data were collected along a 2 km cross-estuary transect, located at Hampton Roads, under different tidal forcing and river discharge between 2004 and 2005. This transect was sampled during three successive neap-spring tidal cycles to assess fortnightly variability (4–12 November 2004, 18–25 April, and 16–23 May, 2005). Four additional surveys that took place during spring tides (23 February and 30 September 2004, 26 January and 23 February 2005) were included to represent seasonal variability.

Continuous velocity measurements and station density profiles were obtained onboard the *R/V Fay Slover* over a period of 12–13 h, with an Acoustic Doppler Current Profiler (ADCP, 600 kHz RD) and a Sea Bird Conductivity–Temperature–Depth (CTD, SBE-25) recorder, respectively. The ship-mounted ADCP collected 1 s pings, which were averaged over 20 s while traversing the transect at ~2 m/s. This gave a horizontal resolution of ~40 m. The vertical bin size was 0.5 m for the data set collected in 2004, and 1 m for the rest. Data were compass-calibrated and corrected by the method of Joyce (1989) using Global Positioning System data. On average, 15 trajectory repetitions were carried out for each data set. The CTD profiles were recorded at 24 kHz at 4 different stations, three of which were along the transect (Fig. 1). The CTD profiles taken from Station 4 were used to calculate the horizontal baroclinic pressure gradient. This station was only occupied during the 2005 surveys.

Hourly time series of mean sea level were obtained from Sewells Point (NOAA station # 8638610), at the entrance of the James River in Norfolk, Virginia. Sea level data were also obtained from the Chesapeake Bay Bridge Tunnel (NOAA, station #

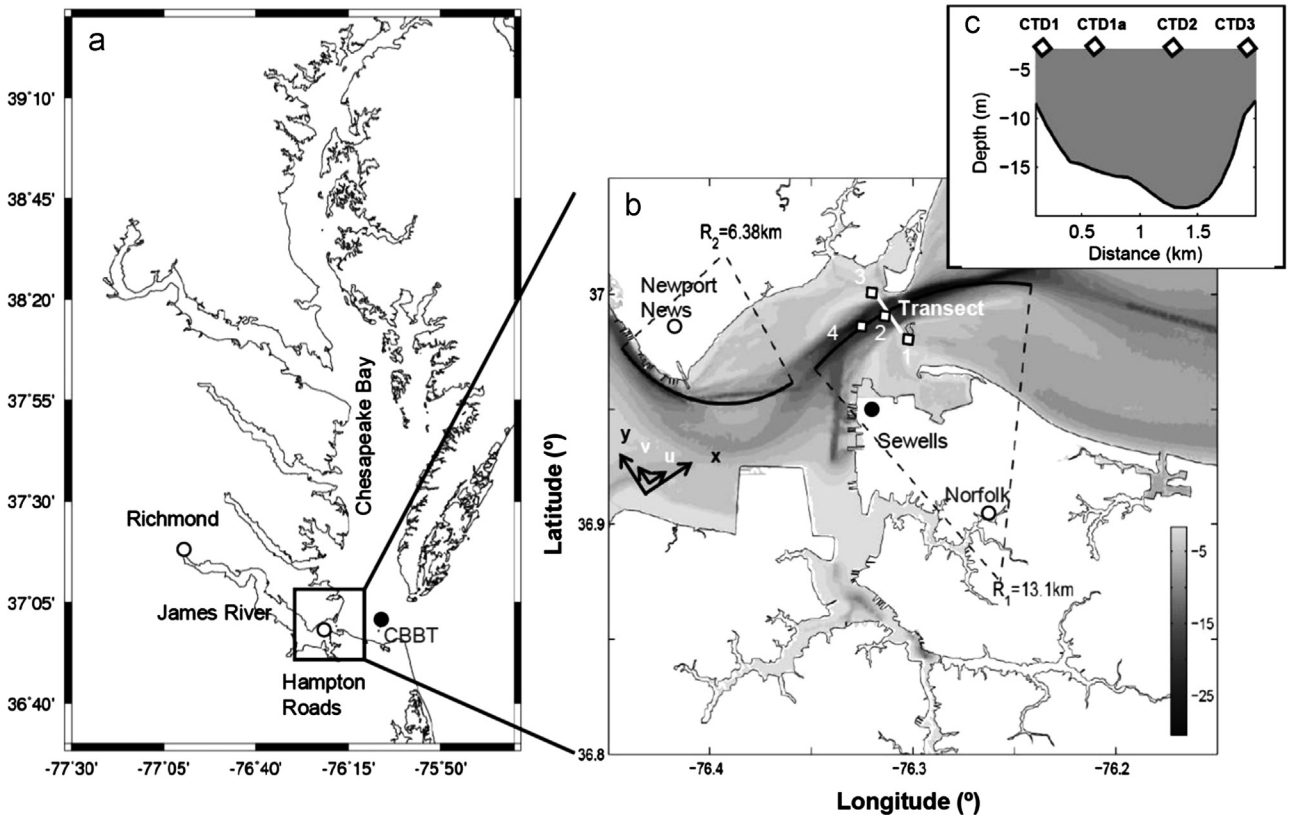



**Fig. 1.** Map of the area of study in the lower James River estuary (Chesapeake Bay) showing the bathymetry, the sampled transect (looking up-estuary), and the five stations where the CTD casts were taken. The two regions of curvature are near Newport News ($R_2$=6.38 km) and near Norfolk ($R_1$=13.1 km). The location of the stations of sea level measurement are denoted by black circles.

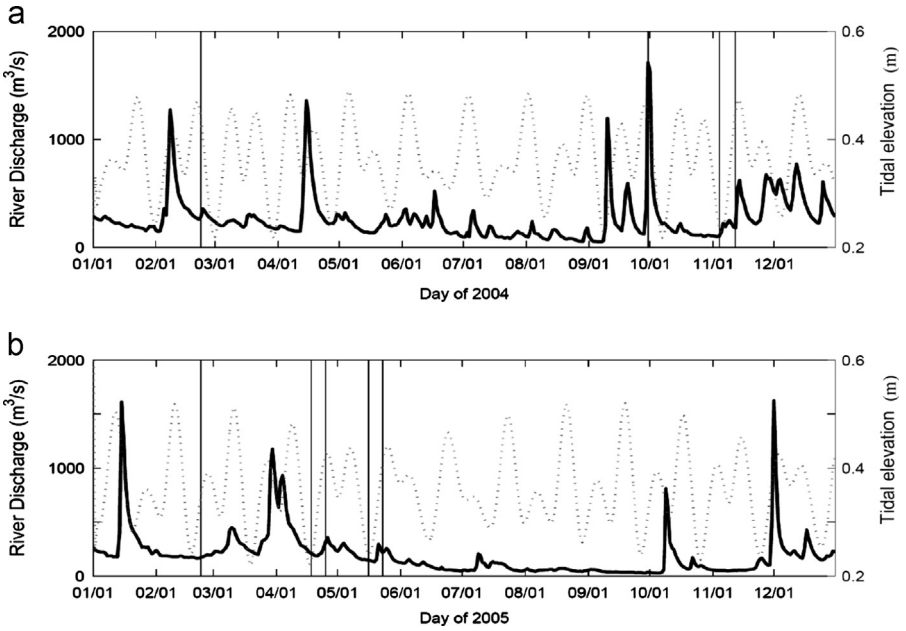



**Fig. 2.** Annual river discharges ($m^3/s$) measured near Richmond and tidal elevations (m) at Sewells Point, Norfolk, VA in 2004 (a), and in 2005 (b).

8638863), which is located between the James River entrance and the Chesapeake Bay entrance. NOAA's National Ocean Service maintains the stations. Historical data for tidal elevations are available on their website (http://tidesandcurrents.noaa.gov). Tidal elevations at Sewells Point (Fig. 2) were used to calculate the temporal variation of barotropic pressure gradient $g\eta_x$, where $g$ is the gravitational acceleration (9.81 $m/s^2$), $\eta$ is the water level elevation, and the subscript $x$ denotes the partial derivative along the estuary. For each survey, the phase difference between the least-squares fitted elevations at Sewells Point and at CBBT was calculated to find the celerity, $c$. Celerity was in the range of 5–8 m/s when $M_2$, $N_2$ and $S_2$ harmonics were included in the fit, and the phase difference of the biggest contributor $M_2$ was used. In order to obtain the temporal variation of $\eta_x$, the following relation was adopted (Lacy and Monismith, 2001)

$$\eta_x = c^{-1}\eta_t \tag{1}$$

with subscript $t$ denoting the partial derivative with respect to time.

The coordinate system used in this study is illustrated in Fig. 1. The $x$ axis coincides with the along-channel direction and is positive toward the mouth of the estuary. Looking into the estuary, the $y$ axis is positive toward the right. The $z$ axis is positive upward. The along-channel direction was identified as that of maximum tidal current variance for the cross section. Time series of current velocities at each depth were rotated by ~25°T to match the coordinate system. The principal component of flow, $u$, represents inflows and outflows and the lateral component $v$ represents the flow aligned with the transect. For all measurements of each transect repetition, the flow components were interpolated onto a regular grid with a resolution of 100 m in the horizontal and 0.5 m in the vertical. The time series of flow components ($u$, $v$) at each grid point were fitted to semidiurnal ($M_2$=12.42 h), quarter-diurnal ($M_4$=6.21 h), and sixth-diurnal ($M_6$=4.14 h) harmonics using a least-squares method:

$$(u,v) = (\overline{u},\overline{v}) + (u',v'),\ \text{where}\ (u',v') = \sum_{j=1}^{m} (u_{Aj}, v_{Aj}) \sin(\omega_j t + u_{\theta j}, v_{\theta j})\ \text{and} \tag{2}$$

$\overline{u}$ and $\overline{v}$ are the subtidal flows; $u'$ and $v'$ are the oscillatory parts of the flow; $m$=3 is the number of harmonics; $u_{Aj}$ and $v_{Aj}$ the amplitudes of the harmonic $j$ of frequency $\omega_j$; $u_{\theta j}$ and $v_{\theta j}$ the phases for each harmonic; $t$ is time. The root-mean-squared error between the fit and the observations was typically $<0.03$ m/s, indicating a good representation by Eq. (2) of actual conditions. The variability explained by the fits was $>92\%$ and it was achieved mostly with the inclusion of three constituents ($M_2$, $M_4$ and $M_6$).

By using the oscillating parts of the velocity components $u'$ and $v'$, the tidal variability of lateral advection $v'u_y'$ was explored. Across-estuary structures for $v'u_y'$ were extracted during peak ebb, peak flood and slack periods. Special attention was given to peak flows because $v'u_y'$ was greatest during these times. Lateral advection was also isolated during slack periods to determine the potential influence of lateral density gradients on advection.

## 4. Results

### 4.1. Density and buoyancy frequency

The density anomaly profiles showed a range between 8 and 30 kg $m^{-3}$ depending mostly on the river discharge influence and tidal amplitude (Figs. 2 and 3). The lowest density values were observed during maximum river discharge at the estuary mouth (30 September 2004 and 18 April 2005). The highest density values were reached on 23 February 2005 and 16 May 2005 when the influence of river discharge at the mouth was small and the tidal amplitude was relatively weak.

The intratidal evolution of stratification $\rho_z$ was explored by calculating buoyancy frequency squared, $N^2$ ($=g/\rho\rho_z$, with positive values indicating stability of the water column, increasing with stratification) for all stations (Fig. 3). Relatively higher stabilities occurred on the northern side (Station #3) during ebb on February 23 2004 and September 30 2004, and during flood on November surveys, with respect to the southern side of the channel (Fig. 3, where peak ebb is denoted by the black dot). Typically, greatest stratification should appear at the end of ebb because of tidal straining, which refers to the interaction between horizontal density gradients and vertical shears in tidal currents (Simpson et al., 1990). Such interaction results in a vertically stratified water column during ebb and a well-mixed water column during flood. This was not observed in these measurements as the most stable

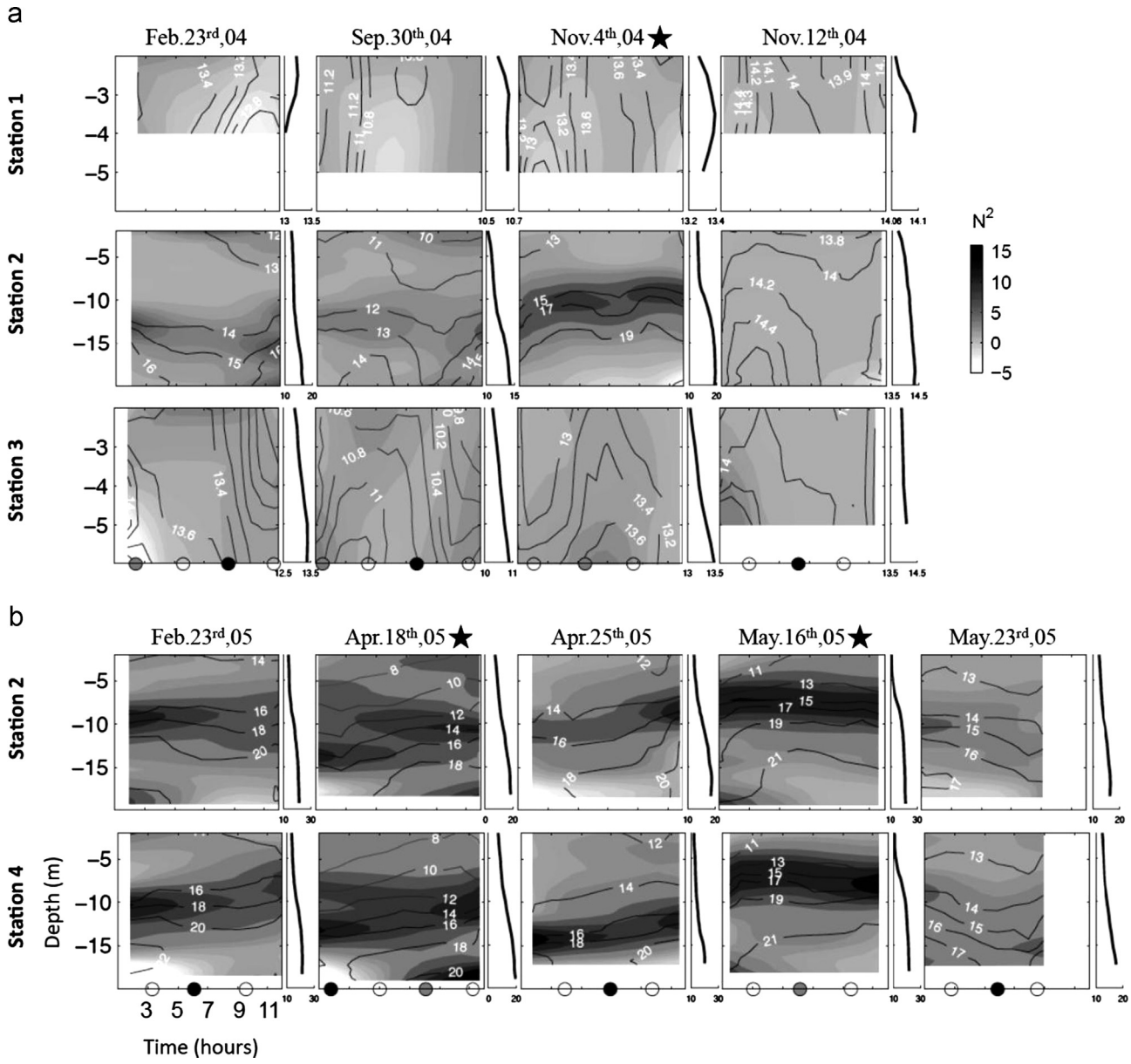



**Fig. 3.** Tidal variation of density anomaly profiles, $\sigma_t$ drawn as contours (kg/m$^3$), mean density profiles $\overline{\sigma}_t$ added right side of each plot (kg/m$^3$) and squared buoyancy frequency, $N^2$ drawn as filled contours ($10^{-3}$ 1/s$^2$) in 2004 (a), and in 2005 (b). Peak ebb, flood and slacks are marked with black, gray and transparent circles, respectively.

water columns were observed during slack after flood. This apparent contradiction can be explained by lateral density gradients ($\rho_y$). Lateral density gradients may cause reverse tidal straining by destroying the stratification produced by longitudinal density gradients ($\rho_x$) under the influence of lateral bathymetry. Phase differences across the cross-section cause a variation in timing of the stratification between the channel and the shoals. In the middle of the water column (Station #2) reversed straining occurred with less stratified ebbs than floods in most of the observations. The time-varying lateral structure of $\rho_y$ on reverse tidal straining was documented at the study area and discussed in terms of its influence on subtidal dynamics (Basdurak and Valle-Levinson, in press). Here, the intratidal influences are discussed.

To analyze the relative importance of $\rho_y$ on stratification, lateral straining ($\rho_y v_z$) and longitudinal straining ($\rho_x u_z$) mechanisms were quantified at the surface (at ~1 m depth) in the vicinity of Station #2 for the 2005 surveys when both along- and across-estuary near-surface salinity data were available. Lateral straining dominated over longitudinal straining in their influence on stratification during all 2005 surveys (Fig. 4). Generally, the peaks of $\rho_y v_z$ appeared at peak ebb or at slack before ebb. Straining $\rho_y v_z$ was reduced under relatively smaller tidal amplitudes (e.g. 23 February and 16 May 2005). However on 18 April 2005, a river discharge of ~1000 m$^3$/s produced a relatively large straining. Decrease in stratification at peak ebbs could be partly attributed to the corresponding $\rho_y v_z$ peaks, which were responsible for carrying the well-mixed shoal water into the channel. Lateral straining peaks at slacks on the other hand might carry well mixed water to the shoals, increasing the stratification in the channel. The depth-variation of lateral straining could not be evaluated because of lack of spatial resolution of density profiles.

Stratification was influenced by tidal intrusion fronts during flood stages of the tidal cycle. Previous studies documented the existence of tidal intrusion fronts in the lower James River (Brubaker and Simpson, 1999; Shen et al., 1999; Shen and Lin, 2006). Tidal intrusion fronts could be evidenced by the increase in near-bed currents along with the enhanced instabilities during peak flood (Figs. 3 and 5). Tidal intrusion fronts could be responsible for reverse tidal straining. Relatively stronger near-bed along-channel currents ($u$) along with

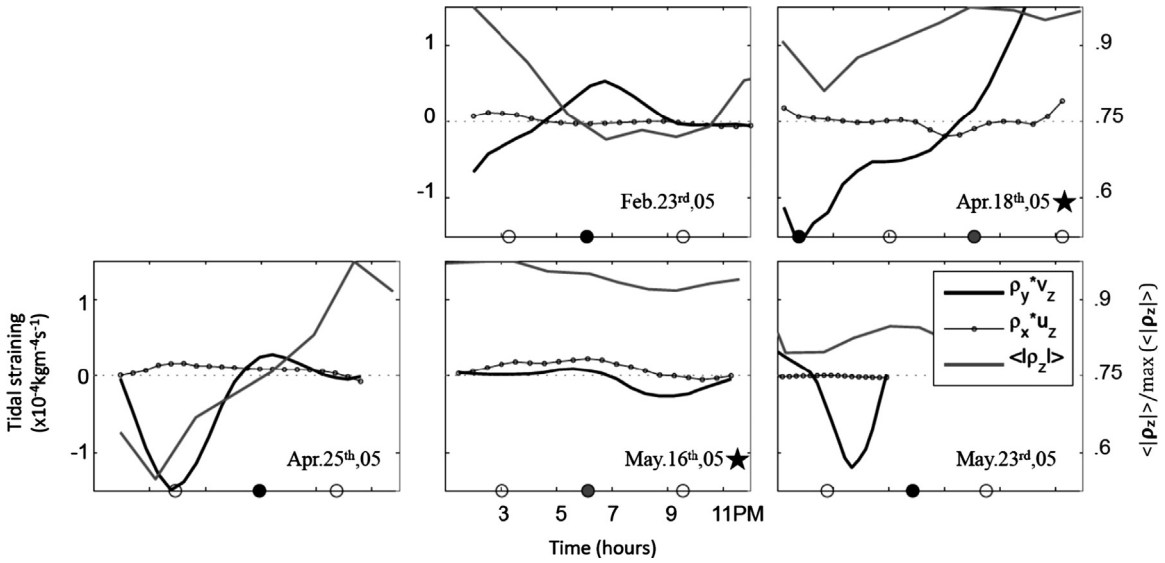



**Fig. 4.** Comparison of the tidal straining mechanisms measured at the surface (Station 2) and stratification in 2005. The thick black line represents the lateral ($\rho_y v_z$) and the thin black line with dots represents the longitudinal ($\rho_x u_z$) straining. The gray line denotes non-dimensional depth averaged absolute values of $\rho_z$ scaled with $y$-axis placed on the right-hand side of the plots. Peak ebb, flood and slacks are marked with black, gray and transparent circles, respectively.

instabilities in the density field, and near-surface lateral flow convergences were evidences of tidal front formation.

### 4.2. Along-channel flows

The intratidal variability in along-channel flow ($u'$) is one of the key aspects in the evolution of lateral advection. The location of the most energetic flow is important because the lateral advective structures mainly emerge from the lateral shear in $u'$. Observations show that the most energetic flows occur at different locations of the cross-section depending on the phase of the tides (Fig. 5). During neap floods, maximum along channel flows tend to occur at mid-depth over shallow regions (i.e., 4 November 2004, 18 April 2005, and 16 May 2005); while at spring tides, maximum flood flows appear at the surface in the channel (rest of the surveys). During ebb, the strongest flows occur over the channel slope (~1 km from the margin) mostly near the surface at both spring and neap tides.

Lateral bathymetry variations play an important role in modifying the currents throughout the transect by causing phase lags from differential friction, and driving lateral flow convergences. Lateral flow convergences intensify along-channel flow near the bed, as observed during ebb in most surveys (Fig. 5a). With the exception of November and 16 May 2005 surveys, the zero-lateral-flow contours coincide with relatively stronger along channel flow at depth ( $< 10$ m). The influence of lateral bathymetry on lateral flow convergences is evidenced by zero-lateral-flow contours being parallel to the bathymetry near the bed (Fig. 5). Valle-Levinson and Li (2000a) observed such behavior in transects across the James River (upstream of Hampton Roads) where there was a phase lag of up to 1 h between shoals and channel.

The intratidal flow structures are not only affected by bathymetry but also by freshwater discharge. Freshwater discharge was influential on $u'$ patterns. Mid-depth maximum flows were observed during peak flood on 30 September 2004 and in the April 2005 surveys (Fig. 2). This was related to the asymmetry in mixing due to river outflow and its interaction with the residual currents, which decelerates flood tidal currents at the surface (Fig. 5b). A similar behavior has been documented at several other estuaries (e.g., Dyer, 1986; Jay and Musiak, 1994; Kim and Voulgaris, 2008).

In addition to the spatial variation of $u'$ from peak ebb to peak flood, there are also tidal asymmetries in the cross-sectionally averaged flows. Along-channel sectionally averaged currents are consistently larger, albeit slightly, during flood than during ebb (Table 1). This is likely a result of the transect sampling not covering the entire cross-section extension from coast to coast, because of navigation restrictions.

### 4.3. Lateral flows

Another key contributor to lateral advection, along with $u'_y$, is lateral flows $v'$ that are responsible for redistributing the along-channel momentum over the cross-section. They are driven by Coriolis, diffusive boundary layers, channel curvature, and by differential advection of along-channel density gradient (e.g., Nunes Vaz and Simpson, 1994; Lerczak and Geyer, 2004). The advection itself contributes on lateral flow as well (Zitman and Schuttelaars, 2012). Channel curvature and differential advection of along-channel density gradients seem to be the main mechanisms driving lateral flows in the study area, as discussed next.

Lateral flow shows intratidal variability having two or three-layer structures (Fig. 5). During peak ebb, the three-layer structure consists mostly of northward flows near the surface and bed, and southward flows at mid-water. A two-layer structure with southward near-surface currents and underlying northward currents is also observed. Two-layer flow results in the development of a counter-clockwise circulation (looking into the estuary) over the entire cross-section. Three-layer flow results in two-gyres in the vertical plane: clockwise near surface and counter-clockwise near bed during peak ebb (looking up-estuary). During peak flood reversed patterns are observed.

The lateral circulation is distorted either by $u'$ or stratification. As the most energetic $u'$ shifts to mid-depth of the water column, the gyres of $v'$ become asymmetric with accelerated northward $v'$ near bed at peak ebb (vice versa at peak flood) (Fig. 5). Such a behavior diminishes the three-layer structure, causing a two-layer near bed flow to dominate over the entire cross-section (e.g., peak ebb on 23 February 2005 and peak flood on 25 April 2005). The influence of stratification on the lateral circulation can be examined on 12 November 2004, when the water column was well mixed. The decrease in stratification causes the gyre formation to be confined to the shoals, leading to net lateral transport during peak ebb and peak flood.

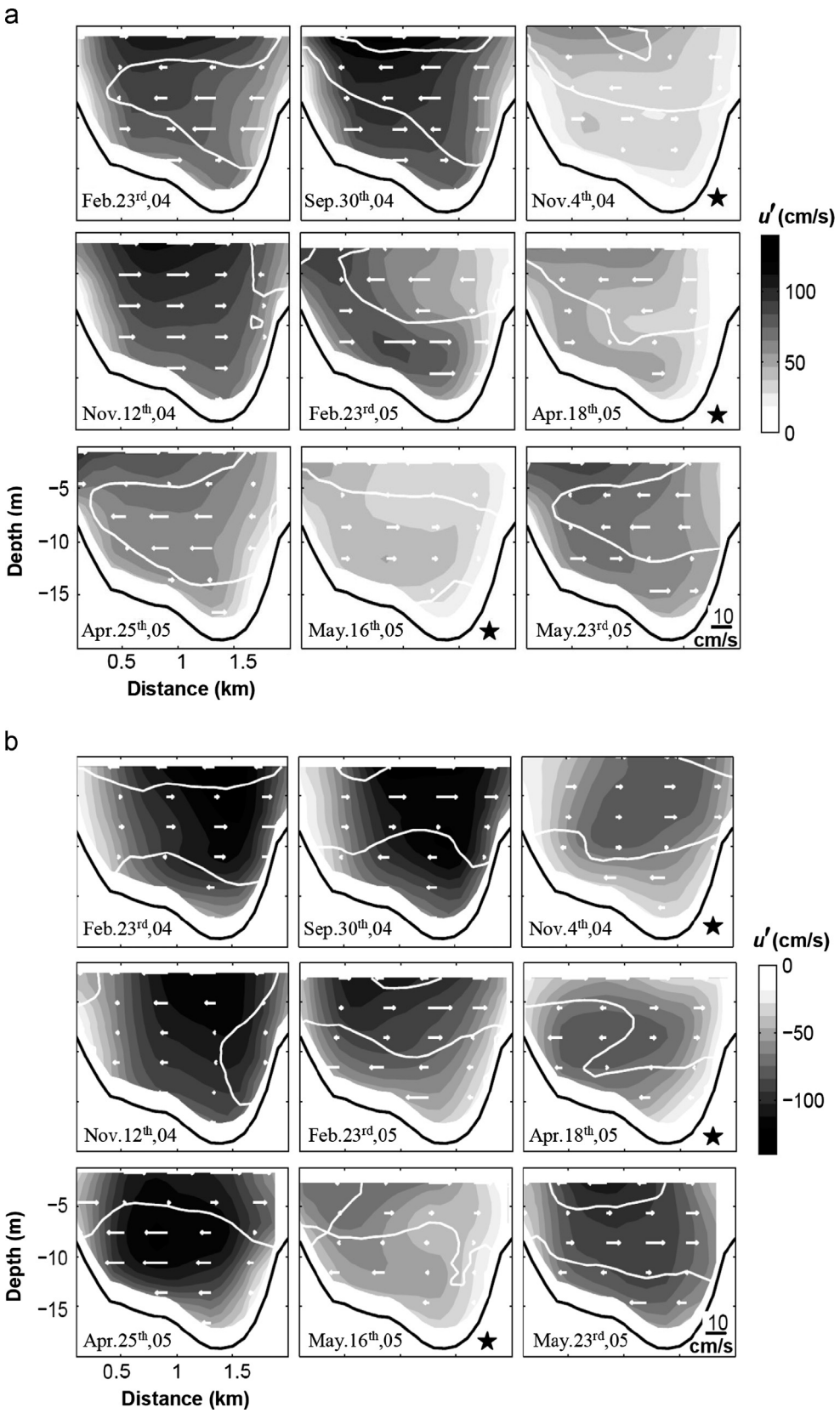



**Fig. 5.** Along and across channel flows (cm/s) at peak ebb (a) and at peak flood (b). White contours stand for zero transverse currents. Across channel flows exclude their depth averages. Stars denote neap tides.

Lateral flows show a flood-ebb asymmetry in terms of both their cross-sectional patterns and their magnitude. The strength of lateral currents is calculated by integrating the absolute values of cross-sectional averages of $v$ over ebb and flood phase of the tide separately.

$$v_p = A^{-1}\left(\int_{ebb}|v'|dA - \int_{flood}|v'|dA\right) \tag{3}$$

**Table 1**
Cross-sectional averages of $u'$ and $v'$ for the entire flood and ebb (cm/s). Tidal asymmetry in $u'$ and $v'$ is represented by $u_p$ and $v_p$ (cm/s), calculated as in Eq. (3). (* denotes neap tides).

| | $\langle\|u'\|\rangle_{flood}$ | $\langle\|u'\|\rangle_{ebb}$ | $\langle\|v'\|\rangle_{flood}$ | $\langle\|v'\|\rangle_{ebb}$ | $u_p$ | $v_p$ |
|---|---|---|---|---|---|---|
| **Feb. 23rd, 04** | 49.6 | 48.6 | 6.1 | 7.7 | −1 | 1.6 |
| **Sep. 30th, 04** | 49.7 | 44.8 | 5.7 | 6.6 | −4.9 | 0.9 |
| **Nov. 04th, 04*** | 33.6 | 27.1 | 4.9 | 4.5 | −6.5 | −0.4 |
| **Nov. 12th, 04** | 54.8 | 51.3 | 7.5 | 13.8 | −3.5 | 6.3 |
| **Feb. 23rd, 05** | 47.1 | 41.3 | 7.1 | 6.1 | −5.8 | −1 |
| **Apr. 18th, 05*** | 31.4 | 28.8 | 5.3 | 5.1 | −2.6 | −0.2 |
| **Apr. 25th, 05** | 61 | 47.1 | 7.3 | 7.5 | −13.9 | 0.2 |
| **May 16th, 05*** | 29.8 | 28.8 | 6.1 | 5.3 | −1 | −0.8 |
| **May 23rd, 05** | 43.8 | 36.6 | 6.8 | 6.9 | −7.2 | 0.1 |

In Eq. (3), the difference between the two phases, $v_p$, is positive if $v$ is stronger during ebb than flood tides, $A$ is the cross-sectional area. Stronger $v$ during flood occurs when the tidal strength is weaker (e.g. 23 February 2005 and neap tides) (Table 1). The rest of the surveys show stronger $v$ during ebb tides. Tidal asymmetry in $v$ affects the spatial distribution of tidally averaged lateral advection, thus its contribution to residual exchange. The tidal asymmetry in $v$ emerges from two mechanisms: (1) $v$ enhancement by lateral density gradients induced by differential advection of along-channel currents, and (2) $v$ suppression by tilted isopycnals; $v$ is stronger during flood than ebb in the absence of morphological features (Lerczak and Geyer, 2004; Scully et al., 2009). The observed ebb-dominant $v$ in this study can be attributed to the intratidal curvature-$\rho_y$ competition as discussed next.

#### 4.3.1. Curvature effects

Curvature of the coastline or of the bathymetry modifies lateral flows through centrifugal accelerations, $CF$ ($=u'^2/R-\langle u'\rangle^2/R$ where $R$ is the radius of curvature and the brackets represent depth average). In the area studied there are two bends: one downstream near Norfolk, which is influential during both flood and ebb phase ($R_1=13.1$ km). The other is upstream at Newport News, which is influential during ebb phase ($R_2=6.4$ km) (Fig. 1). The $CF$ for flood and ebb phase were correspondingly obtained by using $(-1/R_1)$ and $(-1/R_2+1/R_1)$. As a preliminary assessment, curvature-induced lateral flow may be quantified as $6\times|\langle u'\rangle|/R$ when the along channel velocity profile is logarithmic and the eddy viscosity profile is parabolic (Geyer, 1993). The scaling yields lateral flows of ~3–10 cm/s in magnitude. However one should keep in mind the limitations of this scaling as it ignores the asymmetry in the lateral velocities.

In the observations reported here, the $CF$ varied with respect to tidal amplitude showing mostly two-layered structure that was northward near surface and southward near bed, at spring tides (Fig. 6). A three-layered structure occurred during neaps because of the development of non-logarithmic $u'$, with marked intratidal variability. During peak ebb (Fig. 6a), $CF$ was northward at mid-depth and southward in the rest of the water column (opposite during peak flood). There are discrepancies between the distribution of $CF$ and $v'$, such as two-layer $CF$ leading to three-layer $v'$ (Figs. 5 and 6). This can be attributed to lateral density gradients ($\rho_y$), discussed in the next section.

#### 4.3.2. Lateral density gradients

Tidal variability of $\rho_y$ is examined at three locations, over both shoals and in the thalweg. The results are presented as profiles and as surface values by using CTD profiles and underway surface data, respectively (Fig. 7). The tidal variability of $\rho_y$ is presented as surface values because CTD measurements were not available for the 2005 surveys. Lateral density gradients have order of magnitude $O$ ($10^{-4}$–$10^{-3}$) kg/m$^3$/m, showing tidal and spatial variability. In the channel (~1 km from the southern margin), surface lateral density gradients increase at peak ebb and decrease at the end of flood. This decrease in surface $\rho_y$ is accompanied with enhanced near-bed $\rho_y$ at after the end of flood, on 23 February 2004 and 30 September 2004. There is also a lateral change in sign of gradients (i.e., positive gradients driving southward and northward currents near bed and surface, respectively) modifying the lateral circulation induced by $CF$.

Stratification is the key factor determining the mechanism ($CF$ or $\rho_y$) that exerts greater influence on lateral circulation (Buijsman and Ridderinkof, 2008; Nidzieko et al., 2009). All observations, except for 12 November 2004, depict relatively strong stratification which distorts $v'$ through $\rho_y$. The aforementioned discrepancy between the patterns of $v'$ and $CF$ can be explained by spatial and tidal variability of $\rho_y$ under the influence of stratification.

### 4.4. Lateral advective acceleration patterns

During peak currents, the right side (looking up-estuary) of the channel exhibits primarily landward accelerations near the surface and seaward accelerations near the bed (Fig. 8). The opposite behavior is predominantly observed on the left side of the channel.

The specified pattern was more prominent in 2005. This is due to seasonal variations as most 2004 surveys took place in fall whereas most 2005 surveys in spring. This four-celled pattern is disturbed by abrupt lateral changes in bathymetry within the first 1 km of the channel margin, through an increase of the landward accelerations near the bed. Southward surface currents during peak flood and northward surface currents during peak ebb produce landward accelerations on the left side of the channel at the surface (e.g., 23 February, 30 September, 12 November 2004 and May surveys during peak flood; 23 February and 12 November 2004 during peak ebb). During slack periods, seaward accelerations are enhanced at the surface (Fig. 8).

Fortnightly forcing modifies the spatial variability of $v'u'_y$ structures. As tidal forcing increases so does the strength of $v'u'_y$ (i.e. $1–2\times10^{-4}$ m s$^{-2}$ at spring and $0.5\times10^{-4}$ m s$^{-2}$ at neap). Stratification associated with weak tidal amplitudes also affects the $v'u'_y$ patterns. Laterally sheared $v'u'_y$ structures (i.e. landward flow over shoals and seaward in the thalweg at flood) were observed when the water column was well-mixed (e.g. Fig. 8a, 12 November 2004). Furthermore, relatively higher stability is correlated with seaward accelerations over the tidal cycle (Figs. 3 and 8). Seaward accelerations coincide with $N^2$~10 s$^{-2}$ at depths between 10 and 15 m in the mid-channel (Station #2). Thus the vertical shift in the location of the seaward advective accelerations over a tidal cycle can be associated with the pycnocline position (Figs. 3 and 8).

Observations exhibit flood–ebb asymmetry in terms of both magnitude and structure of advective terms. Stronger landward accelerations occur at peak flood than at peak ebb in the April and May surveys (opposite in the rest of the observations) (Fig. 8). The tidal asymmetry in lateral advection arises from the aforementioned spatial variability of the strongest $u'$ and $v'$ over the cross-section.

### 4.5. Phase and amplitude of semidiurnal and fourthdiurnal currents

Lateral advective acceleration patterns can be examined according to the relative phase and amplitude of tidal currents. Spatial variability of phase and amplitude was analyzed separately for semidiurnal ($\theta_{M2}$ and $A_{M2}$ and) and fourthdiurnal ($\theta_{M4}$ and $A_{M4}$ ) harmonics. In most surveys, $A_{M2}$ decreases from surface to bottom because of bed friction (Fig. 9a). Exceptions to such behavior can be explained by lateral advective accelerations dominating over

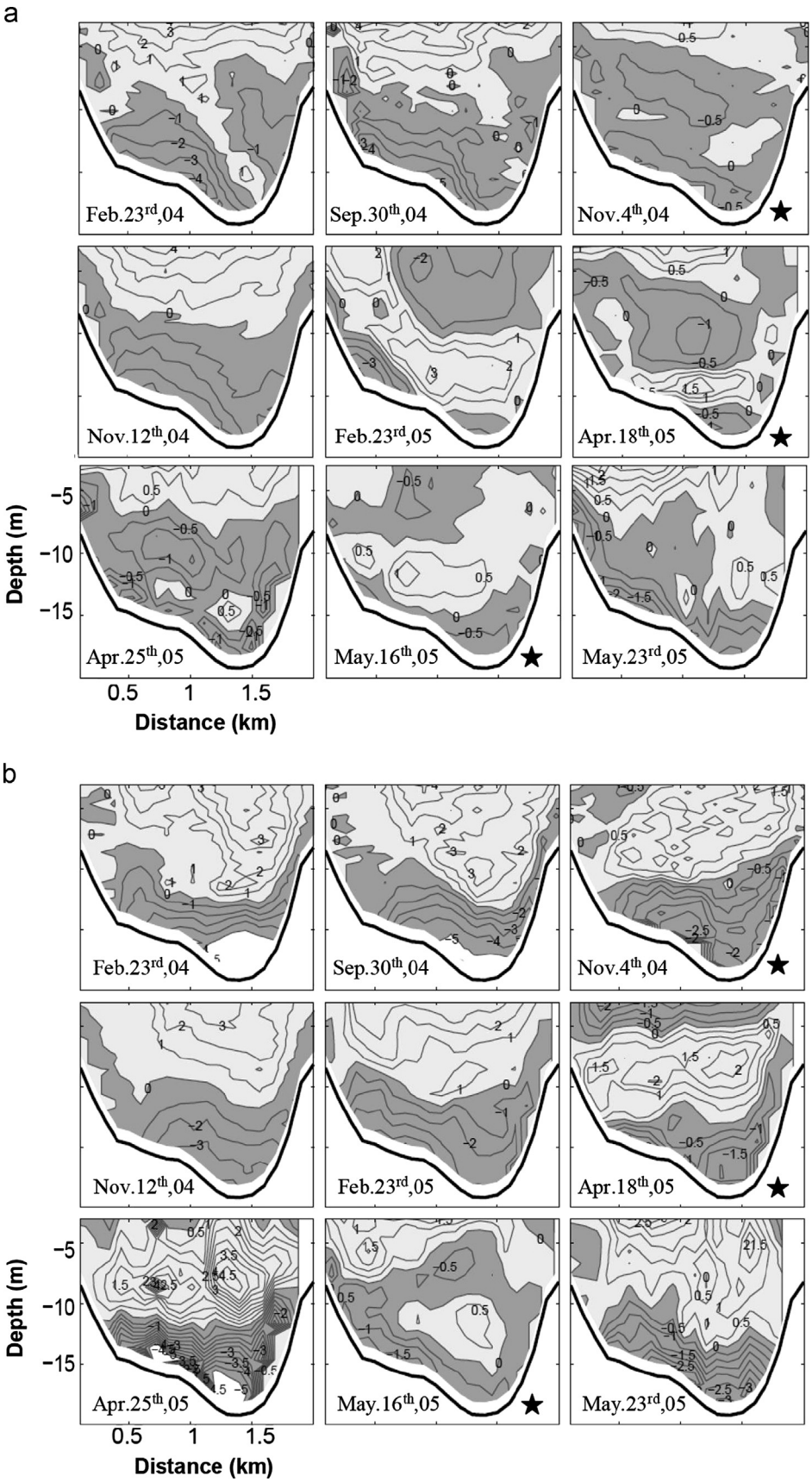



**Fig. 6.** Centrifugal acceleration ( $\times 10^{-3}$ cm/s$^2$) across the section at peak ebb (a), and at peak flood (b). Stars denote neap tides. Positive values (light-shaded contours) are northward.

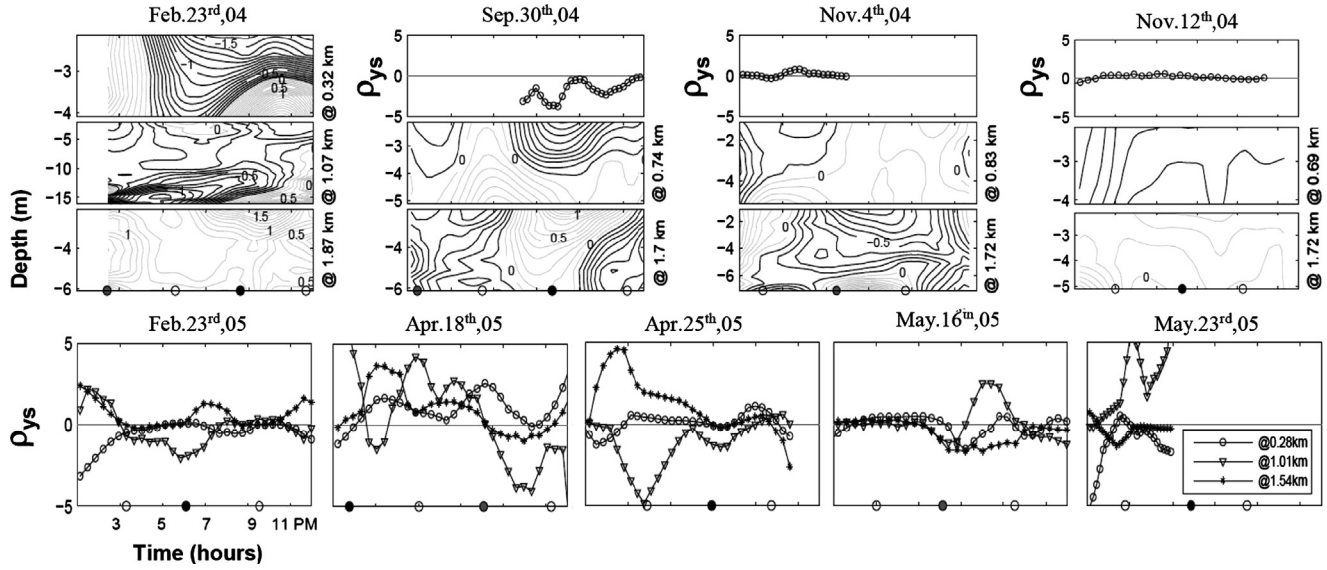



**Fig. 7.** Tidal variation of lateral density gradients over the water column ($\rho_y$, denoted with no-marker contours and $10^{-4}$ kg/m$^3$/m contour intervals were used) and at the surface ($\rho_{ys}$). Lateral density gradients were calculated between the available CTD stations. Their exact locations are stated on the *y*-axis as distances from the southern edge of the transect. Peak ebb, flood and slacks are marked with black, gray and transparent circles, respectively.

friction (e.g., neap tides of 4 November 2004 and 18 April 2005 at 0.5–1 km away from the left- or southern- end where there is an abrupt change in bathymetry). The correlation between $A_{M2}$ patterns and lateral advective accelerations is shown by the dominant phase of $v'u'_y$ (Fig. 8). The zones with relatively stronger $v'u'_y$ coincide with regions of decreased $A_{M2}$ near bed. Furthermore, $A_{M2}$ and $\theta_{M2}$ structures are influenced by stratification. A mid-depth decrease in $A_{M2}$ at Station #2 (e.g., 4 November 2004, 23 February 2005, 18 April and 16 May 2005) can be attributed to the pycnocline (Figs. 3 and 9). A similar but more prominent relation exists between $A_{M4}$ and pycnocline position. Vertical lag in $\theta_{M2}$ shows variability along the transect: decreasing over the shoals due to friction (fast response to tidal changes), and increasing with stratification at neaps (slow response to tidal changes above a stratified region). Enhanced mixing in all three CTD stations on 12 November 2004 reduces the vertical lag in $\theta_{M2}$ close to zero throughout the cross-section (Figs. 3 and 9a ). Still, lateral lags of ~20° persist from the channel to the shoals.

Distributions of $A_{M4}$ and $\theta_{M4}$, which must be determined by nonlinear tidal distortions (e.g. Huijts et al., 2009), appear to be correlated with lateral advective structures (Figs. 9b and 8). Landward accelerations coincide with increased $A_{M4}$ (~30 cm/s), whereas seaward accelerations occur when enhanced $A_{M4}$ (~30 cm/s) and $\theta_{M4}$ (~360°) coexist. The tidal and spatial variation of lateral advective patterns is further discussed in the next section in light of other mechanisms contributing to the momentum balance.

### 4.6. Momentum balance

The relative importance of lateral advection in the along-channel momentum balance is quantified over a tidal cycle. Neglecting horizontal friction, longitudinal advection, and vertical advection, for the sake of comparison, the balance can be simplified as:

$$u'_t + v'u'_y - fv' = -g\eta'_x - (g/\rho_0)\int_z^{\eta}\rho'_x dz + (A_z u_z)'_Z \qquad (4)$$

where subindices are the partial derivative of corresponding variables with respect to space ($x$, $y$, and $z$) and time ($t$), $f$ is the Coriolis parameter ($8.8\times10^{-5}$ s$^{-1}$), $\rho_0$ is a reference density (~1010 kg/m$^3$), and $A_z$ is the vertical eddy viscosity (in m$^2$/s). The balance expressed in Eq. (4) includes the influence of local, lateral advective, Coriolis, barotropic and baroclinic pressure gradient accelerations, as well as vertical mixing/friction, in that order.

A Richardson number ($R_i$) -dependent turbulence closure (Pacanowski and Philander, 1981) is used to determine the vertical eddy viscosity coefficient, $A_z$. This closure performs best among the low order schemes (Nunes Vaz and Simpson, 1994) and is given by

$$A_z = 0.01(1+5R_i)^{-2} + 10^{-4}, \text{ where } R_i = \frac{(g/\rho_0)\rho_z}{(u_z)^2 + (v_z)^2} \text{ and} \qquad (5)$$

$R_i$ stands for gradient Richardson number, a dimensionless ratio between buoyancy and shear production of turbulence.

Absolute values of all terms in Eq. (4) are averaged over the cross-section in order to compare the tidal variation in strength of each term (Fig. 10). The highest vertical mixing rates were found for the 2004 surveys, which remained relatively high throughout the tidal cycle. Differences between 2004 and 2005 surveys are related to fall conditions in 2004 and spring conditions in 2005. Coriolis accelerations of lateral flows $f\,v'$ have the weakest impact on the along-estuary momentum balance as they are $O$ ($10^{-3}$–$10^{-4}$) cm/s$^2$. Their trend, however, is similar to the tidal trend of lateral advection $v'u'_y$. This similarity indicates that $v'$ sets the trend of lateral advection but $u'_y$ determines its magnitude, in a cross-sectionally averaged sense. Lateral advective accelerations have the same order of magnitude as the pressure gradient $O$ ($10^{-2}$–$10^{-3}$) cm/s$^2$. They are strongest just after peak flood, at peak flood and at peak ebb, and weakest at the slack before flood. Relatively large flood–ebb asymmetry of $v'u'_y$ (~0.5 order of magnitude difference) can be attributed to enhanced baroclinity due to river currents (30 September 2004, 4 November 2004, and 18 April 2005) (Figs. 2 and 10). The increase in asymmetry related to river discharge was also documented by Chant (2002).

The spatial structure in $v'u'_y$ can be gleaned by examining their relative contribution at certain phases of the tidal cycle (Figs. 8 and 10). Seasonal variation in friction (i.e., stronger during 2004 than 2005) affects the $v'u'_y$ patterns consistently throughout the tidal cycle. The difference between spring and neap cycles (laterally sheared $v'u'_y$ at neaps and vertically sheared $v'u'_y$ at springs) is more prominent during 2004, when friction is relatively stronger. Vertically sheared advective structure is enhanced by baroclinic gradients at slack after ebb on 18 April 2005 and at peak ebb on 23 May 2005. This is restricted to the vicinity of the thalweg, where the gradients were calculated. A decrease in baroclinicity at peak ebbs on 23 February

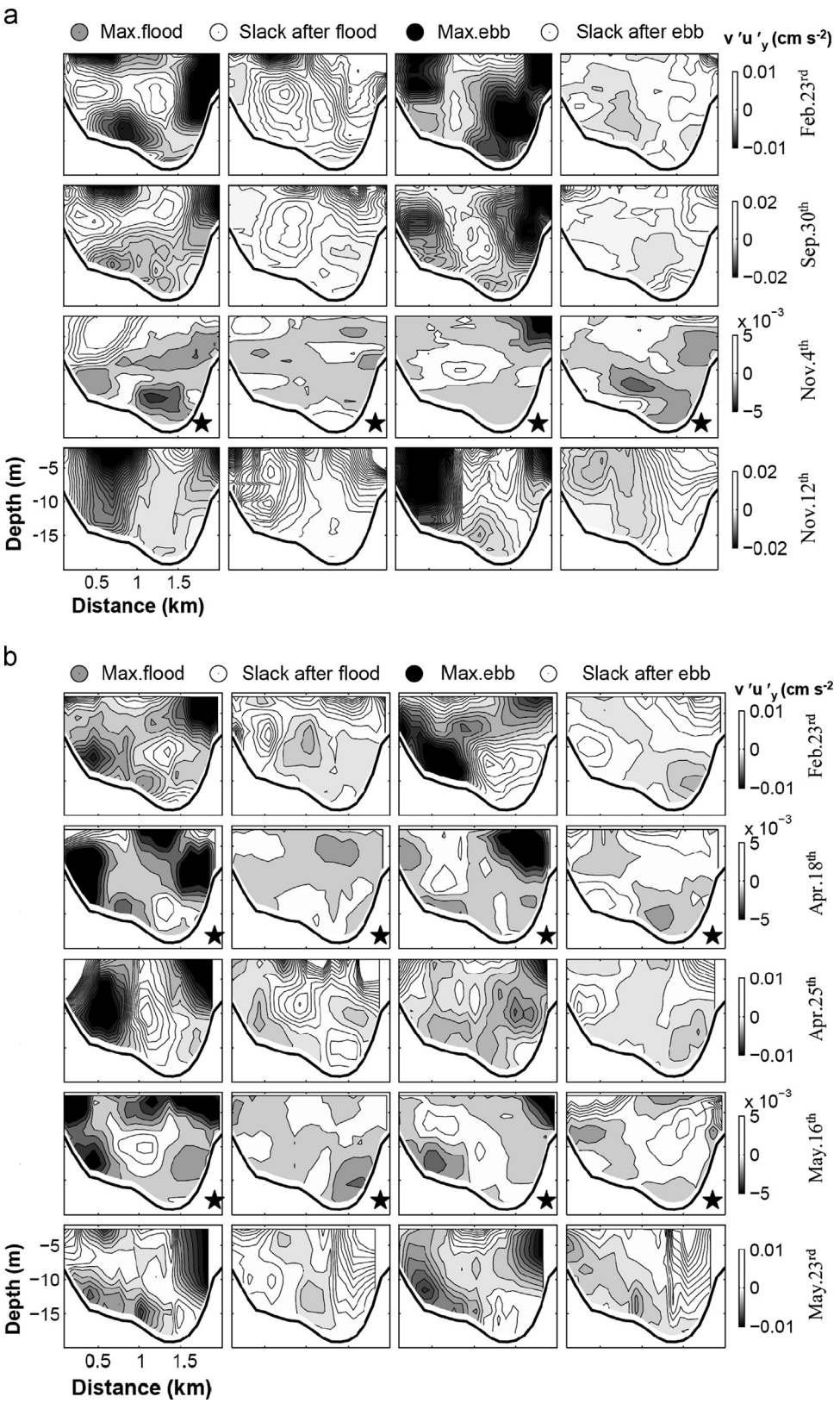



**Fig. 8.** Tidal variation of lateral advection, $-v'u'_y$ (cm/s$^2$) in 2004 (a), and in 2005 (b). Positive values denote seaward accelerations. Stars denote neap tides.

2005 and 25 April 2005, and at slacks on 23 May 2005, diminishes the vertical shears. A four-celled structure emerges as $v'u'_y$ dominates over the other terms. This is seen at peak flood on 4 November 2004 and 18 April 2005; and at peak ebb on 23 February 2005 and 23 May 2005.

### 4.7. Comparison to idealized model results

Observed lateral advective acceleration patterns were compared to idealized model results of Huijts et al. (2009). The model was able to depict separate contributions to lateral advection from

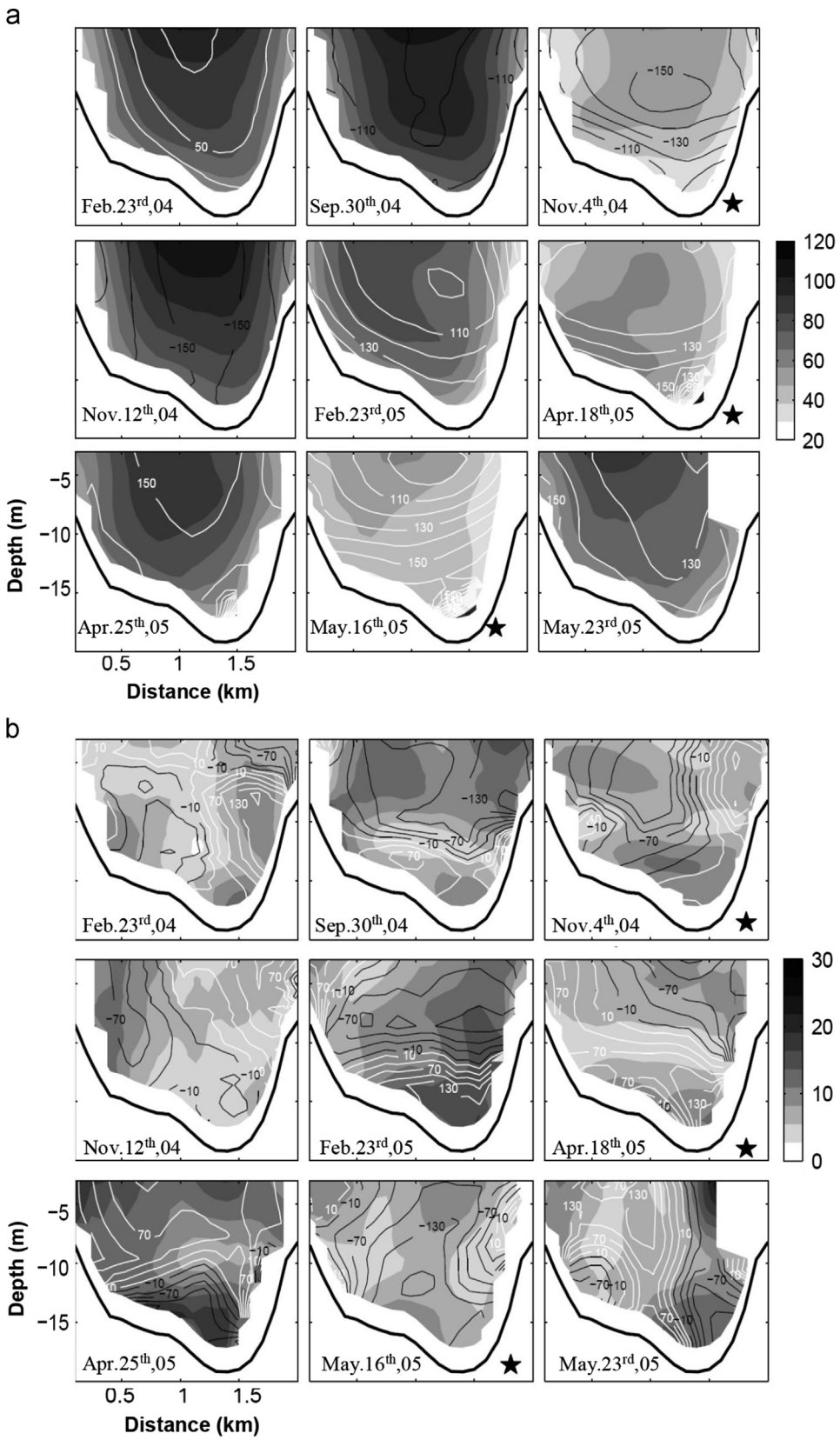



**Fig. 9.** The amplitude (filled contours in cm/s) and angles (contours in degrees) of semidiurnal (a); fourth-diurnal (b). Black contours represent angles between 180° and 360°. Stars denote neap tides.

Coriolis deflection of along channel flow, from friction, and from lateral density gradients. The dominant features of observations mostly agreed with idealized model predictions, although there were some discrepancies. In particular, the four-celled structure, which was found in most surveys either during peak ebb or peak flood, was predicted by Huijts et al. (2009). They described

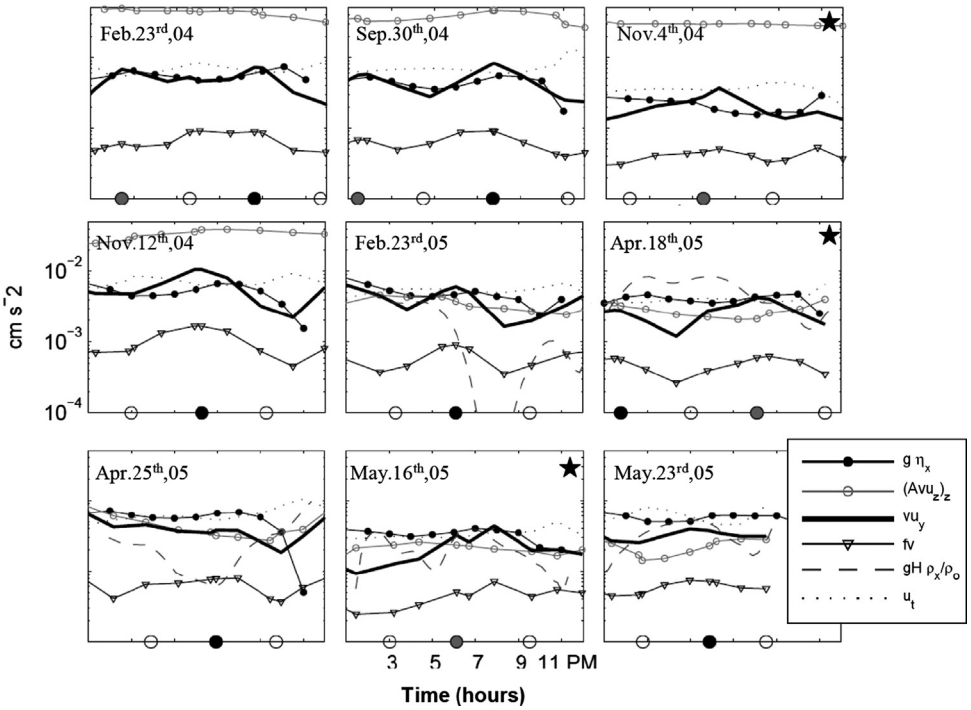



**Fig. 10.** Cross-sectional averages of the absolute value of the terms in the along-channel momentum equation over a tidal cycle (Eq. (5)). Black, gray and transparent circles represent peak ebb, peak flood and slacks, respectively.

tidal-cycle patterns of lateral advection as a four-celled spatial structure: two-layer circulation similar to gravitational circulation on the left side and reversed circulation on the right side of the channel, when looking up-estuary in the Northern Hemisphere (Fig. 11a). They concluded that such structure is most robust during peak ebb and peak flood. They also analyzed the influence of $\rho_y$ and resulting three-layer lateral advective patterns (landward at mid-depth, seaward at surface and bed), which was intensified over the channel slopes during slack periods (Huijts et al., 2011). A three-layer structure (e.g. Fig. 11b) was observed in some of the surveys over relatively shallow bathymetry (within the first 1 km from the southern end). Enhanced near-surface seaward accelerations originating over the channel slopes during slack on 30 September 2004 and 4 November 2004 could be attributed to this mechanism (Fig. 9). However $\rho_y$ can change sign along the transect, which may reverse the circulation described. High water slack tides on 25 April 2005 featured positive $\rho_y$ near Station #1 and negative $\rho_y$ near Station #2, which resulted in the expected three-layer pattern on the northern end and a reversed three-layer pattern on the southern end of the transect. Discrepancies could be attributed to lateral and longitudinal variations in bathymetry, which distort the density field both laterally and vertically. Moreover, the model ignores vertical variability of density gradients ($\rho_z$ is constant throughout the water column).

The interaction between bathymetry and density field triggers tidal asymmetries in $u'$ and $v'$, causing $v'u'_y$ to be dominant either during flood or ebb. This tidal asymmetry in $v'u'_y$ affects the along-channel flow over subtidal time scales, causing nonlinearity-induced residual flows. The subtidal lateral advection ($\overline{v'u'_y}$, where the overbar denotes tidal average) and thus the subtidal along-channel flow patterns, essentially represent the influence of the dominant tidal phase (Basdurak and Valle-Levinson, 2011).

The observations presented here show that lateral advection is influential to the intratidal dynamics of the estuary studied. It is expected that longitudinal advection $u'u'_x$ and vertical advection $w'u'_z$ also play a role, as demonstrated by Huijts et al. (2009, 2011). However, analytical models of tidal dynamics in semienclosed basins have shown that tidal flows resulting from the balance among local accelerations, pressure gradient and friction, without advective accelerations, represent observations remarkably well (e.g. Huijts et al., 2006; Winant, 2007; Arnott et al., 2012). It is likely then, that advective accelerations must be canceled out by other dynamical agents such as asymmetries in internal mixing, which has been shown to be also a sizable dynamic term (e.g. Cheng et al., 2011; Burchard and Schuttelaars, 2012). Future observational studies will have to explore this possible cancellation by quantifying advection and tidal asymmetries in mixing. Basdurak and Valle-Levinson (in press) have made a first attempt, which suggests such cancellation but the temporal and spatial resolution of the data is insufficient to arrive at a firm conclusion.

## 5. Conclusion

The dynamics behind along-channel tidal flow accelerations consisted of friction, pressure gradient and lateral advection. Lateral circulation was mainly driven by centrifugal acceleration from morphology and lateral density gradients. Lateral density gradients played an important role, particularly during stratified conditions, in the channel and intensified over regions of increased gradients in lateral bathymetry.

Intratidal variation of lateral advection ($v'u'_y$) was explored in detail for the first time in a coastal plain estuary with observations. Its contribution to the along-channel momentum balance throughout the tidal cycle was found to be of the same order of magnitude as the baroclinic pressure gradient. Its impact on along-channel flow was strongest during or just after the peak flood and weakest at the end of ebb.

A section-wide, roughly defined four-cell circulation, emulating analytical model results, was observed with flood tides favoring the seaward accelerations either at the southern side near surface or the northern side near bed (looking up-estuary), whereas ebb tides favored landward accelerations in the rest of the channel. The discrepancies between observations and model results could

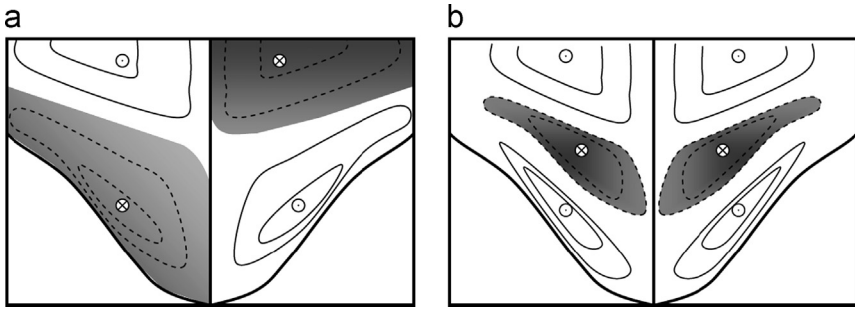



**Fig. 11.** Schematic representation of idealized model results for lateral advection triggered by (a) Coriolis deflection of along-channel flow-four celled structure (adopted from Huijts et al., 2009); (b) lateral density gradients-three layer lateral advective pattern (adopted from Huijts et al., 2011). Darker shades represent the landward accelerations.

be attributed to the complex nature of the bathymetry and its interaction with density gradients, which caused asymmetries in $v'u'_y$. Although tidal flows can be reproduced reliably with an analytical solution in which accelerations are provided by pressure gradient and friction (e.g. Huijts et al., 2006; Winant, 2007) without the need for advective accelerations, the tidal asymmetries in advective accelerations provide relatively large forcing for the subtidal flow and should be canceled by another dynamic mechanism such as tidal asymmetries in mixing.

## Acknowledgments

This research was funded by NSF projects OCE 0551924, OCE 0825876 and OCE 1065990. This paper was completed while AVL was a visiting fellow at Utrecht University. Many people were involved in the survey ADCP collection including W. Ashley, B. Belmont, E. Chapman, J. Desai, K.C. Filippino, R. Moody, S. Husrevoglu, L. Iliffe, R.C. Kidd, D. Narvaez, M. Ott, A. Pinones, D. Salas, and A. Sanford.

## References

Arnott, K., Valle-Levinson, A., Luther, M., 2012. Friction-dominated exchange in a Florida estuary. Estuarine, Coastal and Shelf Science 113, 248–258.

Basdurak, N.B., Valle-Levinson, A., 2011. The influence of nonlinear advective terms on estuarine exchange at a Chesapeake Bay tributary. Journal of Physical Oceanography 42 (10), 1617–1634.

Basdurak, N.B., Valle-Levinson, A. Lateral structure of tidal asymmetry invertical mixing and its impact on exchange flow in a coastal plane estuary. Continental Shelf Research, http://dx.doi.org/10.1016/j.csr.2013.05.005, in press.

Brubaker, J.M., Simpson, J.H., 1999. Flow convergence and stability at a tidal estuarine front: acoustic Doppler current observations. Journal of Geophysical Research 104 (C8), 18257–18268.

Buijsman, M.C., Ridderinkhof, H., 2008. Variability of secondary currents in a weakly stratified tidal inlet with low curvature. Continental Shelf Research 28, 1711–1723.

Burchard, H., Schuttelaars, H., 2012. Analysis of tidal straining as driver for estuarine circulation in well mixed estuaries. Journal of Physical Oceanography 42, 261–271.

Chant, R.J., 2002. Secondary circulation in a region of flow curvature: Relationship with tidal forcing and river discharge. Journal of Geophysical Research 107 (C9), 3131, http://dx.doi.org/10.1029/2001JC001082.

Chatwin, P.C., 1976. Some remarks on the maintenance of the salinity distribution in estuaries. Estuarine and Coastal Marine Science 4, 555–566.

Cheng, P., Valle-Levinson, A., 2009. Influence of lateral advection on residual currents in microtidal estuaries. Journal of Physical Oceanography 39, 3177–3190.

Cheng, P., Valle-Levinson, A., de Swart, H.E., 2011. A numerical study of residual circulation induced by asymmetric tidal mixing in tidally dominated estuaries. Journal of Geophysical Research 116, C01017, http://dx.doi.org/10.1029/2010JC006137.

Dyer, K.R., 1986. Coastal and Estuarine Sediment Dynamics. John Wiley, Hoboken, N.J..

Joyce, T.M., 1989. On in situ calibration of shipboard ADCPs. Journal of Atmospheric and Oceanic Technology 6 (1), 169–172.

Geyer, W.R., 1993. Three-dimensional tidal flow around headlands. Journal of Geophysical Research 98, 955–966.

Hansen, D.V., Rattray, M., 1965. Gravitational circulation in straits and estuaries. Journal of Marine Research 23, 104–122.

Huijts, K.M.H., Schuttelaars, H.M., de Swart, H.E., Valle-Levinson, A., 2006. Lateral entrapment of sediment in tidal estuaries: an idealized model study. Journal of Geophysical Research 111, C12016, http://dx.doi.org/10.1029/2006JC003615.

Huijts, K.M.H., Schuttelaars, H.M., de Swart, H.E., Friedrichs, C.T., 2009. Analytical study of the transverse distribution of along-channel and transverse residual flows in tidal estuaries. Continental Shelf Research 29, 89–100.

Huijts, K.M.H., de Swart, H.E., Schramkowski, G.P., Schuttelaars, H.M., 2011. Transverse structure of tidal and residual flow and sediment concentration in estuaries: Sensitivity to tidal forcing and water depth. Ocean Dynamics 61, 1067–1091, http://dx.doi.org/10.1007/s10236-011-0414-7.

Jay, D.A., Musiak, J.D., 1994. Particle trapping in estuarine tidal flows. Journal of Geophysical Research 99 (C10), 445–461.

Kim, Y.H., Voulgaris, G., 2008. Lateral circulation and suspended sediment transport in a curved estuarine channel, Winyah Bay, South Carolina, USA. Journal of Geophysical Research 113, C085050, http://dx.doi.org/10.1029/2007JC004509.

Lacy, J.R., Monismith, S.G., 2001. Secondary currents in a curved, stratified, estuarine channel. Journal of Geophysical Research 106 (C12), 31283–31302.

Lerczak, J.A., Geyer, W.R., 2004. Modeling the lateral circulation in straight, stratified estuaries. Journal of Physical Oceanography 34, 1410–1428.

Nidzieko, N.J., Hench, J.L., Monismith, S.G., 2009. Lateral circulation in well-mixed and stratified estuarine flows with curvature. Journal of Physical Oceanography 39 (4), 831–851.

Nunes Vaz, R.A., Simpson, J.H., 1994. Turbulence closure modeling of estuarine stratification. Journal of Geophysical Research 99, 16143–16160.

Officer, C.B., 1976. Physical Oceanography of Estuaries (and associated coastal waters). John Wiley, New York465.

Pacanowski, R.C., Philander, S.G.H., 1981. Parameterization of vertical mixing in numerical models of tropical oceans. Journal of Geophysical Research 103, 15657–15666.

Pritchard, D.W., 1956. The dynamic structure of a coastal plain estuary. Journal of Marine Research 15 (1), 33–42.

Shen, J., Boon, J.D., Kuo, A.Y., 1999. A modeling study of a tidal intrusion front and its impact on larval dispersion in the James River estuary. Estuaries 22, 681–692.

Shen, J., Lin, J., 2006. Modeling study of the influences of tide and stratification on age of water in the tidal James River. Estuarine, Coastal and Shelf Science 68, 101–112.

Simpson, J.H., Brown, J., Matthews, J., Allen, G., 1990. Tidal straining, density currents and stirring in the control of estuarine stratification. Estuaries 13, 125–132.

Scully, M.E., Geyer, W.R., Lerczak, J.A., 2009. The influence of lateral advection on the residual estuarine circulation: a numerical modeling study of the Hudson River Estuary. Journal of Physical Oceanography 39, 107–124.

Valle-Levinson, A., Li, C., 2000a. Convergence of lateral flow along a coastal plain estuary. Journal of Geophysical Research 105 (C7), 17045–17061.

Valle-Levinson, A., Wong, K.C., Lwiza, K.M.M., 2000b. Fortnightly variability in the transverse dynamics of a coastal plain estuary. Journal of Geophysical Research 105 (C2), 3413–3424.

Winant, C.D., 2007. Three-dimensional tidal flow in an elongated, rotating basin. Journal of Physical Oceanography 37, 2345–2362.

Zitman, T.J., Schuttelaars, H.M., 2012. Importance of cross-channel bathymetry and eddy viscosity parameterization in modeling estuarine flow. Ocean Dynamics 62, 603–631.